Classification of Neurons in the Adult Mouse Cochlear Nucleus: Linear Discriminant Analysis

Paul B. Manis[1], Michael R. Kasten[1], Ruili Xie[2]

[1]Department of Otolaryngology/Head and Neck Surgery, The University of North Carolina at Chapel Hill
[2]Department of Otolaryngology, The Ohio State University, Columbus, OH

Text Pages:

Figures: 7

Tables: 1

Corresponding Author:

Paul B. Manis, Ph.D.
Dept. of Otolaryngology/Head and Neck Surgery
The University of North Carolina at Chapel Hill
B027 Marsico Hall
125 Mason Farm Road
Chapel Hill, NC 27599-7070

Tel: 919 843 9318
Email: paul_manis@med.unc.edu

Disclaimers:

This work has not been peer-reviewed.

The authors have no competing interests to declare.

Research reported in this preprint was supported by the National Institute on Deafness and other Communicative Disorders of the National Institutes of Health under grants R01 DC004551 to PBM and R03 DC013396 to RX.

The content is solely the responsibility of the authors and does not necessarily represent the official views of the National Institutes of Health.

Abstract

The cochlear nucleus (CN) transforms the spike trains of spiral ganglion cells into a new set of sensory representations that are essential for auditory discriminations and perception. These transformations require the coordinated activity of different classes of neurons that are embryologically derived from distinct sets of precursors. Decades of investigation have shown that the neurons of the CN are differentiated by their ion channel expression and intrinsic excitability. In the present study we have used linear discriminant analysis (LDA) to perform an unbiased analysis of measures of the responses of CN neurons to current injections to mathematically separate cells on the basis of both morphology and physiology. Recordings were made from cells in brain slices from CBA mice and a transgenic mouse line, NF107, crossed against the Ai32 line. For each cell, responses to current injections were analyzed for spike rate, spike shape (action potential height, afterhyperpolarization depth, first spike half-width), input resistance, resting membrane potential, membrane time constant, hyperpolarization-activated sag and time constant. Cells were filled with dye for morphological classification, and visually classified according to published accounts. The different morphological classes of cells were separated with the LDA. Ventral cochlear nucleus (VCN) bushy cells, planar multipolar (T-stellate) cells, and radiate multipolar (D-stellate) cells were in separate clusters, and were also separated from all of the neurons from the dorsal cochlear nucleus (DCN). Within the DCN, the pyramidal cells and tuberculoventral cells were largely separated from a distinct clusters of cartwheel cells. DCN cells fell largely within a plane in the first 3 principal axes, whereas VCN cells were in 3 clouds approximately orthogonal to this plane. VCN neurons from the two mouse strains were slightly separated, indicating either a strain dependence or the differences in slice preparation methods. We conclude that cochlear nucleus neurons can be objectively distinguished based on their intrinsic electrical properties, but that such distinctions are still best aided by morphological identification.

Introduction

Neurons of the mammalian cochlear nucleus exhibit a variety of responses to intracellular current injection, reflecting the distinct expression of collections of ion channels amongst different classes. However, even within a class, such as bushy cells, individual cells may express specific conductances at different magnitudes (Rothman and Manis 2003b, a; Cao and Oertel 2011), leading to diversity in excitability features such as action potential threshold, action potential height, and rheobase. In spite of this variability, cells of a given morphological class appear to possess common properties that have been used to identify cells on the basis of their electrical signatures alone (Oertel 1983; Wu and Oertel 1984; Oertel et al. 1990; Zhang and Oertel 1993a, b, 1994; Manis et al. 1994; Kuo et al. 2012; Xie and Manis 2017).

Quantitative methods for identifying cell classes have been explored in the context of the myriad interneuronal populations in cortex (Druckmann et al. 2013), within the olfactory bulb (Tavakoli et al. 2018) and across neuronal populations throughout the brain (Tripathy et al. 2015). These methods rely on systematic measurement of distinct features of intrinsic excitability such as action potential shape, firing rates, passive membrane measures, and responses to hyperpolarization, and have used principal components analysis (PCA), support vector machine model, or stepwise linear regressions. Within the cochlear nucleus, application of an hierarchical clustering analysis to *in vivo* single unit data provided evidence for partial separation of unit response types in the gerbil AVCN (Typlt et al. 2012), although further analysis (using PCA) suggested that there was extensive overlap between cell classes.

Here we apply linear discriminant analysis (Rao 1948) to the problem of separating cell classes in the cochlear nucleus based on intrinsic excitability. Whereas PCA separates classes by finding the axes that maximize the variance within a data set, and does not rely on labels, LDA maximizes the separation between classes, utilizing label (e.g., class) information. We find that LDA is an effective tool for segregating the cell classes based on their excitability, while also suggesting that there is either overlap between the properties of some of the classes, or that they may not be entirely morphologically distinguishable. Such a classification tool should be useful in future studies of the excitability of cochlear nucleus neurons following hearing loss as a way of objectively assessing how the excitability of neurons changes.

Methods

Whole cell tight-seal recordings were made in brain slices from adult CBA (P28-69) and NF107::Ai32 (P31-166) mice. The NF107::Ai32 mice are the F1 cross of the NF107 mouse line, originally from the GENSAT Consosrtium (Gong et al. 2003), and the channel rhodopsin (ChR2) expressing line Ai32 (Madisen et al. 2012), and so are on a mixed C57Bl/6J and FVB background. The ChR2 was not activated during these experiments. CBA mice were of either sex, whereas the NF107::AI32 mice were only males, as the Cre driver is carried on the Y chromosome.The data from the CBA mice were taken from a previous series of studies (Xie and Manis 2013, 2017). Data from the NF107::Ai32 mice were taken from unpublished work (Kasten, Ropp and Manis, in preparation). The CBA slices were prepared following anesthesia (100 mg/kg ketamine

121 and 10 mg/kg xylazine), and decapitation, with slicing in warm ACSF. The NF107::Ai32
122 slices were prepared using the same anesthesia followed by transcardial perfusion with
123 an NMDG-based solution (Ting et al. 2014). Electrodes contained 126 K-gluconate, 6
124 KCl, 2 NaCl, 10 HEPES, 0.2 EGTA, 4 Mg-ATP, 0.3 Tris-GTP, and 10 Tris-
125 phosphocreatine, with pH adjusted to 7.2 with KOH and recordings were made with a
126 MultiClamp 700B (Molecular Devices) amplifier, low-pass filtered at 6kHz, and digitized
127 at 10-20 kHz with 16-bit A-D converters (National Instruments). Stimulus presentation
128 and acquisition were controlled by either a custom Matlab® program or by acq4
129 (Campagnola et al. 2014). All animal procedures were approved by the University of
130 North Carolina Institutuional and Animal Care Committee (protocols 12-253, 15-253 and
131 18-160).
132 For each cell, responses to current injections (100-500 msec duration, ranging from -1
133 to 4 nA) were analyzed. Data from either acquisition program were converted to a
134 common format for analysis by Python (V3.6) scripts. Passive measures included input
135 resistance (from the slope of the current-voltage relationship just below rest), resting
136 membrane potential, membrane time constant (measured from responses to small
137 hyperpolarizing current steps that produced 2-10 mV voltage deflections), the
138 magnitude of the hyperpolarization sag (Fujino and Oertel 2001) and the time constant
139 for the sag measured near -80 mV. Active measures included action potential height
140 (measured from rest to action potential peak), first spike half-width (measured at half the
141 action potential height from rest), afterhyperpolarization depth (measured from rest to
142 the first afterhyperpolarization), an adaptation index measured near firing threshold (see
143 below), the number of rebound spikes after hyperpolarizing steps, the coefficient of

variation of interspike intervals, and the slope of the firing rate versus current curve for the first 3 current levels above threshold. Cells were filled with dyes (AlexaFluor 488 for CBA mice; tetramethylrhodamine biocytin for the NF107:Ai32 mice) for morphological classification, and visually classified according to published accounts, based on digital images and image stacks collected at low (4X) and high (40-63X) power either during or immediately after each cell was recorded.

Adaptation was measured for the lowest two levels of current that elicited spikes as:

$$\frac{-2}{N}\sum_{i=0}^{i=N}\left(\frac{t_i}{t_d}-0.5\right)$$

Where t_i is the time of the ith spike in the trace, t_d is the trace duration, and N is the number of spikes. This measure ranges from -1 to 1. Neurons that fire regularly without adaptation throughout the trace will have an index of 0. Neurons that fire preferentially only at the onset of the trace will have an index of 1, whereas those that fire near the end of the trace will have an index of -1. Thus, bushy cells will have an index of 1, stellate cells and tuberculoventral cells will usually have an index near 0, and pyramidal cells may have a negative index, depending on the delay to the first spike. Note that this measure depends on the current level that is used relative to the spike threshold, as well as the current duration. The adaptation measured at the threshold current was found to be uninformative in preliminary analyses, and so the only adaptation computed from the next higher current that evoked spikes was used.

All absolute voltage measurements are corrected for a -11 mV junction potential for the K-gluconate electrodes. All other voltage measurements are differential (action potential

height from peak to the minimum of the following AHP) and are independent of the junction potential.

Computed measures were then analyzed using LDA and PCA using standard libraries in Python (scikit-learn v0.20, Python 3.6), and in R (3.5, using the packages DisplayR and flipMultivariates).

Results

The discharge patterns of cochlear nucleus neurons have been reported in a series of studies over the years from multiple laboratories using similar, but not identical recording conditions. Figure 1 shows the intrinsic physiology of example cells from six major morphological classes as recorded in our dataset. Briefly, bushy cells (Figure 1A) fire 1-3 action potentials at the onset of depolarizing current injections, and are silent thereafter (Oertel 1983; Wu and Oertel 1984). At higher current levels, oscillatory membrane responses, which may represent axonally initiated action potentials, are sometimes visible. In response to hyperpolarizing pulses, bushy cells can show a slow sag in membrane potential, and following the hyperpolarizing step can generate an anodal break spike. The planar multipolar cells (Figure 1B) fire regularly in response to depolarizing current injections, and also show a slow sag in response to hyperpolarizing current steps; they can also show anodal break spikes (Fujino and Oertel 2001; Xie and Manis 2017). Radiate multipolar cells also fire regularly in response to depolarization,

189 sometimes exhibiting an adapting spike train. They show a rapid sag in response to
190 hyperpolarization, and frequently have anodal break spikes. As noted previously (Xie
191 and Manis 2017), radiate multipolar cells also may fire only at the onset of a weak
192 depolarizing current pulse. Pyramidal (fusiform) cells of the dorsal cochlear nucleus fire
193 regularly (Hirsch and Oertel 1988; Manis 1990; Zhang and Oertel 1994), and may have
194 a long delay to the first spike or a long first interspike interval (Manis 1990; Kanold and
195 Manis 1999; Street and Manis 2007). In the adult mice studies here, these cells do not
196 show a prominent sag, but do show a rapidly activating rectification in response to
197 hyperpolarizing steps, which is likely generated by Kir channels (Leao et al. 2012).
198 Cartwheel cells show mixed single-spiking regular firing and burst firing (Zhang and
199 Oertel 1993a; Manis et al. 1994). The tuberculoventral neurons show regular firing, and
200 often have trains of rebound spikes after hyperpolarization (Zhang and Oertel 1993c;
201 Kuo et al. 2012). The principal cell database included 18 bushy cells, 32 planar
202 multipolar cells, 32 radiate multipolar cells, 38 pyramidal cells, 12 cartwheel cells, and
203 31 tuberculoventral cells. Additional cell classes (all from the DCN) had too few cells for
204 effective classification. These included 1 “Type-B” cell (Lorente de No 1981), 1 chestnut
205 cell (Weedman et al. 1996), 7 giant cells, 2 “horizontal bipolar” cells (small neurons in
206 the pyramidal cell layer of the DCN with a bipolar morphology where the moderately
207 spiny dendrites reside mainly within the pyramidal cell layer), 2 molecular layer stellate
208 cells (Apostolides and Trussell 2014), 3 unipolar brush cells (Weedman et al. 1996;
209 Mugnaini et al. 2011), and 3 cells that could not clearly be identified on comparison with
210 the literature. These were not included in the analyses.
211

212 In order to classify the principal cell types, we extracted a set of measurements from the
213 current-voltage and spiking responses (N = 163 cells). These are illustrated in Figures 2
214 and 3. Figure 2 summarize the passive properties of the cells (columns) against the cell
215 types (rows). From this, differences in the resting membrane potential, input resistances
216 and time constants can be appreciated between the groups. In addition, measurements
217 of the time constant of the hyperpolarizing sag, and a previously-used measure (Fujino
218 and Oertel 2001), the B/A sag ratio, also show clear differences between the cells, with
219 neurons from the DCN generally showing weaker I_h.
220
221 Figure 3 shows measures of action potential shape and firing properties. Again,
222 population-based distinctions are evident, such as the relatively small and wide action
223 potentials of bushy cells, and the tendency of tuberculoventral and some cartwheel cells
224 to show rebound responses, and the wide coefficient of variation of firing of the
225 cartwheel cells. The firing rate slope measured near threshold also was lowest for
226 bushy, pyramidal and cartwheel cells, and highest for the planar and radiate multipolar
227 cells, and tuberculoventral cells.
228
229 Next, we submitted the data to a LDA, using all of the parameters measured in Figures
230 2 and 3. Data were first standardized for each measure before being submitted to the
231 LDA. The standardization rescaled the individual measurements for each measurement
232 type so that it had a zero mean and a unit standard deviation. Figure 4 illustrates the
233 first 3 components of the LDA, with each cell colored by its classified type, in 3 views
234 (Figure 4A, B, C). The LDA effectively separated the different types of cells into distinct

spaces. The bushy and cartwheel cells were the most separated from the remainder of the regular firing cells. Interestingly these two cell groups did not form tight clusters, suggesting some diversity in their properties. The pyramidal and tuberculoventral cells were clustered next to each other, although with minimal overlap. The radiate and planar multipolar cells formed two slightly overlapping clusters that were largely separate from all other cell classes. Note that although most of the bushy, planar and radiate multipolar cells were recorded in CBA mice, those cells recorded from the NF107::Ai32 mice (FVB and C57Bl/6 backgrounds; solid symbols) were close to the measures of the CBA populations, although they were slightly separated in one of the first 3 axes, as more clearly seen in Figure 4D, where only cells from the VCN are shown. Cross-validation of the LDA yielded an estimated accuracy of 0.75 (+/- 0.24).

We also submitted the data set to a standard principal components analysis, following the same standardization across cells for each measure (Figure 5). In this case, the supervisory classifier (cell morphology) was not used in the initial classification. The PCA resulted in clusters of cells from the same morphological class, but these had greater overlap than with the LDA. Cross-validation of the PCA data yielded a low accuracy of 0.17 (+/- 0.079).

In order to determine which measures provided the most information in the LDA classification, we performed the LDA using combinations of measures, from individual measures through all available measures, and estimated the accuracy of the classification across all cells by dividing the data into training and testing sets. The

accuracy as a function of the number of combined measures is shown in Figure 6. As expected, the accuracy improves as new measures are added, up until about 6 parameters, at which point the accuracy plateaus. However, the overall *worst* accuracy continues to improve as more measures are added. The black line indicates the mean of the best 5 combinations of measures. From this we conclude that some of the measures are possibly redundant and that some measures may be non-informative. With 7 or 8 combined measures (where the largest number of combinations was tested), AP height, R_{in}, RMP, τ_h and I_{rate} occurred together in each of the 5 most accurate runs. Similar, but not identical distributions were present for 8 combined measures. Note that the accuracy of each point includes a standard deviation estimate (not shown) as it is the result of multiple runs with different subsamples of training and test cells, so the best measures can vary with an arbitrary threshold, and there is no single “optimal” set. With the number of cells in the sample and the large number of parameters, the SD can be 15-20% of the mean value.

To further investigate those factors that drove the prediction accuracy, we performed the same analysis using the R package flipMultivariates. Table 1 summarizes the prediction accuracy by cell type, and provides mean measures for each of the parameters. Although all parameters provide a significant contribution (r^2) to the separation, the five that accounted for the largest proportions of the variance ($r^2 > 0.50$) were the AP height, AP half width, the adaptation measure, the coefficient of variation of interspike intervals, and the firing rate slope (Irate). However, all of the measures showed a significant contribution.

Figure 7 plots the overall prediction accuracy against the observed classifiers. Although the overall accuracy was fairly high (87.1%), there were several confounds. The most common of these was radiate vs. planar multipolar, which occurred in about 25% of the cells in these groups. The next most common confound was misclassifying planar multipolar and tuberculoventral cells as pyramidal cells, followed by pyramidal cells being misclassified as tuberculoventral and planar multipolar cells. As these cells all fire regularly, and have similar measures on other properties, this is not surprising.

Discussion

We find that cells thoughout the cochlear nucleus can be classified by firing patterns, action potential shapes, and responses to hyperpolarizing steps, as well as their morphology. Although not surprising given the long history of the identification of various electrophysiological features as identifying characteristics of different morphological cell classes, the extension of these comparisons across classes that fire regularly, and the consistency of these measures in a population of cells taken from adult mice extends the previous observations made in younger mice. In addition, these results suggest that cells can be reasonably classified, at least coarsely, according to their electrophysiological signatures.

We found that the linear discriminant analysis can be used to classify cells based on 12 measured electrophysiological parameters with ~80% success, although there was little

304 improvement when using more than 7 parameters. This requires that the LDA
305 coefficients be estimated from a standardized (training) set of cells before application to
306 an unidentified population. The selection of the training cell, and the quality of that data
307 set, is critical to the success of the technique. Cell morphology should be positively
308 identified, and ambiguous cases discarded, although it is essential to include a full
309 range of cell properties in each class. The measurements should be complete and
310 precise for each cell. Our data set has three limitations in part because it was collected
311 as part of a different experiments. The first is that due to different levels of
312 hyperpolarizing current injection, the voltages reached with hyperpolarizing pulses were
313 not consistent across cells, so that the estimates of the magnitude of the
314 hyperpolarizing sag are influenced by the variability of the voltages reached. The
315 second is that for depolarizing pulses, not all cells reached saturation of their firing
316 rates. For this reason, we did not include maximal firing rates as a measure, but rather
317 focused on the discharge patterns closer to spike threshold. A third limitation is that the
318 current steps near spike threshold were, in some cells, too coarse to precisely define a
319 threshold current. These limitations partly reflect the different input resistances of
320 neurons, as an example, hyperpolarizing pulses strong enough to damage
321 tuberculoventral cells often fail to hyperpolarize pyramidal cells to -80 mV.
322
323 Classification errors principally occurred between cell classes with similar firing patterns,
324 such as planar and radiate multipolar cells, and between pyramidal and tuberculoventral
325 cells. In addition, the TV and bushy cells show significant dispersion in the first 3
326 dimensions of the LDA. This may indicate variability in the intrinsic excitability of these

327 cell classes as noted before (Francis and Manis 2000; Cao et al. 2007; Kuo et al. 2012),
328 or possibly the existence of distinct subclasses. This dispersion was also evident in the
329 unsupervised PCA analysis. Substantially larger datasets of identified cells from
330 individual strains would be needed to clarify the existence of such subclasses in the
331 electrophysiology. An improvement in the classification would be expected to result from
332 the inclusion of additional parameters such as maximal firing rates and the time courses
333 of synaptic events. In addition, in our data set there was some overlap between the
334 planar and radiate multipolar cells. This may in part reflect the limitations of
335 classification for these two similarly firing cell types, but may also indicate the limitations
336 of our morphological classification method, which was qualitative and relied on
337 fluorescent images of the cells collected during the experiments. The qualitative
338 morphological classification of DCN neurons is much easier, so the overlap between the
339 pyramidal and tuberculoventral cells probably represents the limitations of the
340 measurement parameters used, although it could also reflect a true confluence of
341 intrinsic excitability.
342
343 Part of the dispersion in the VCN cell classes may reflect strain or preparation
344 differences, as the cells from CBA mice were slightly offset from those from the
345 NF107::Ai32 mice along the second LDA component. The strain difference is
346 reminiscent of the differences in HCN channels seen in bushy, planar multipolar and
347 octopus cells between ICR and a knockout on a hybrid 129S and C57Bl/6 background
348 (Cao and Oertel 2011). This raises a cautionary flag that the LDA should be trained on
349 data acquired from cells recorded from animals of the same genetic background (and

350 age and preparation techniques) if it is to be used to categorize cells from a novel data

351 set.

352 **Figure Legends**

353

354 Figure 1. Examples of discharge patterns for 6 classes of cochlear nucleus neurons (A.
355 Bushy; B. planar multipolar; C. radiate multipolar; D. pyramidal; E. cartwheel; F.
356 tuberculoventral), and passive responses, for different levels of current injection. Red
357 dots indicate spikes evoked by current injection.

358

359 Figure 2. Summary of passive measurements from responses to hyperpolarizing current
360 pulses across the population of CN neurons. RMP: resting membrane potential; R_{in}:
361 input resistance; τ_m: membrane time constant; τ_h: time constant of repolarizing sag from
362 traces near -80 mV; B/A: steady-state over peak voltage deflection for hyperpolarizing
363 sag (from Fujino and Oertel, 2001). The ordinate indicates the population density based
364 on the kernel density estimate (blue line). The histograms shows the distribution of
365 values from the population cells for each type and measure.

366

367 Figure 3. Summary of action potential shape and firing patterns across the population of
368 CN neurons. AP Peak: action potential peak potential; APHW: action potential half-
369 width; AHP: action potential afterhyperpolarization; Adaptation: adaptation calculated
370 from the response to a suprathreshold current injection; Rebound: count of rebound
371 action potential after the end of the hyperpolarizing current injection; CV: coefficient of
372 variation of interspike intervals; Irate: slope of the current-firing relationship for current
373 levels just above spike threshold. The ordinate indicates the population density based

374 on the kernel density estimate (blue line). The histograms show the distribution of
375 values from the population cells for each type and measure.
376
377 Figure 4. LDA with supervised clustering by cell morphology. A. The first 3 (largest)
378 LDA components are shown in a perspective view. The axes represent the projections
379 of each cell on to the 3 largest components from the standardized data (zero mean, unit
380 standard deviation; therefore there are no units). Note the clear separation of the bushy
381 cell and cartwheel cells populations from the rest of the CN neurons. Although the other
382 populations are close together, they are also separated as can be appreciated by
383 comparing the different views. Cells from CBA mice are shown with open symbols; cells
384 from the NF107 mice are shown with closed symbols. B, C. Two other perspective
385 views (rotated) of the same data as in A. D. A view of the data for the VCN cells only
386 (bushy, planar multipolar and radiate multipolar) for clarity. This is the same perspective
387 view as panel C.
388
389 Figure 5
390 Principal components analysis (PCA) on the same data set; the PCA method is not
391 supervised by cell type, and so the results depend only on factors that maximize the
392 variance. The PCA successfully separated the cell classes, but did not have good
393 accuracy. Four views are shown, in the same format as Figure 4.

Figure 6

Accuracy of separation for different number of combined measures, using the LDA separation score for each set of measures. All 12 measures were considered in all possible combinations in groups from 1 to 12 (the number of combinations are shown above the data), and each combination is plotted as a point along the ordinate representing the number of combinations. The mean score is indicated by the red line. The average of the best 5 scores for each combination set are plotted as a black line. In general, including more measures improves the accuracy of the separation of groups.

Figure 7

Prediction accuracy table (confusion matrix) by cell type. The most frequent mis-classifications occurred amongst cells with similar general firing patterns, such as planar and radiate multipolar cells, and pyramidal and tuberculoventral cells. This table was generated in R using data from all 12 measures. The numbers in each box indicate the proportion of correct classifications for each cell type.

Table 1

Measure	Bushy	Cartwheel	Radiate Multipolar	Pyramidal	Planar multipolar	Tuberculo-ventral	R^2	p
RMP (mV)	**-62.5**	**-75.2**	**-63.1**	**-68.5**	**-62.9**	**-67.9**	0.41	**<0.001**
τ_m (ms)	**1.29**	5.25	**2.83**	**8.0**	4.9	**12.7**	0.41	**<0.001**
R_{in} (MΩ)	**27.5**	79.6	**60.1**	68.8	87.9	**155.6**	0.39	**<0.001**
τ_h (ms)	**27.5**	56.9	**12.1**	51.0	39.4	**74.4**	0.32	**<0.001**
B/A	0.50	**0.95**	**0.39**	0.59	0.63	**0.71**	0.28	**<0.001**
AP Height (mV)	**-27.6**	2.9	**5.9**	**2.2**	**6.0**	**-6.9**	0.62	**<0.001**
AP Width (ms)	**1.32**	**0.83**	**0.28**	**0.40**	**0.27**	**0.35**	0.73	**<0.001**
AP AHP (mV)	**-57.6**	**-53.8**	**-68.3**	-64.6	**-68.9**	-62.1	0.31	**<0.001**
AP Adaptation	**0.96**	0.22	0.21	**0.10**	**0.05**	**0.13**	0.62	**<0.001**
AP Rebound (N)	0.33	1.37	1.17	1.37	1.63	**11.41**	0.25	**<0.001**
CV	N/A	**0.71**	**0.07**	0.10	**0.05**	0.14	0.65	**<0.001**
I_{rate} (spikes/nA)	**5.8**	768	1158	4.12	1248	1148	0.52	**<0.001**
Correct Predictions (%)	94.4	83.3	81.3	92.1	81.3	90.3		

Relations between the predictors and each cell class, indicating the number of correct predictions overall, and for each class. The top predicting variabiles (largest R^2 values) are highlighted. N = 163 cases used in estimation. Null hypotheses: two-sided; multiple comparisons correction: False Discovery Rate correction applied simultaneously to entire table.

Table Caption

Table 1

Relations between the predictors and each cell class, indicating the number of correct predictions overall, and for each class. The top predicting variabiles (largest R2 values) are highlighted. N = 163 cases used in estimation. Null hypotheses: two-sided; multiple comparisons correction: False Discovery Rate correction applied simultaneously to entire table.

427

428 **References**

429

430 Apostolides PF, Trussell LO (2014) Superficial stellate cells of the dorsal cochlear
431 nucleus. Front Neural Circuits 8:1–9. doi: 10.3389/fncir.2014.00063
432 Campagnola L, Kratz MB, Manis PB (2014) ACQ4: an open-source software platform
433 for data acquisition and analysis in neurophysiology research. Front Neuroinform
434 8:3. doi: 10.3389/fninf.2014.00003
435 Cao X-J, Oertel D (2011) The magnitudes of hyperpolarization-activated (Ih) and low-
436 voltage-activated potassium (IKL) currents co-vary in neurons of the ventral
437 cochlear nucleus. J Neurophysiol 106:630–640. doi: 10.1152/jn.00015.2010
438 Cao X-J, Shatadal S, Oertel D (2007) Voltage-sensitive conductances of bushy cells of
439 the Mammalian ventral cochlear nucleus. J Neurophysiol 97:3961–3975. doi:
440 10.1152/jn.00052.2007
441 Druckmann S, Hill S, Schurmann F, et al (2013) A hierarchical structure of cortical
442 interneuron electrical diversity revealed by automated statistical analysis. Cereb
443 Cortex 23:2994–3006. doi: 10.1093/cercor/bhs290
444 Francis HW, Manis PB (2000) Effects of deafferentation on the electrophysiology of
445 ventral cochlear nucleus neurons. Hear Res 149:91–105. doi: 10.1016/S0378-
446 5955(00)00165-9
447 Fujino K, Oertel D (2001) Cholinergic modulation of stellate cells in the mammalian
448 ventral cochlear nucleus. J Neurosci 21:7372–7383. doi: 10.1523/JNEUROSCI.21-
449 18-07372.2001
450 Gong, Shiaoching, Zheng C, et al (2003) A gene expression atlas of the central nervous

451 system based on bacterial artificial chromosomes. Nature 425:917–925. doi:
452 10.1038/nature02033
453 Hirsch JA, Oertel D (1988) Intrinsic properties of neurones in the dorsal cochlear
454 nucleus of mice, in vitro. J Physiol 396:535–548. doi:
455 10.1113/jphysiol.1988.sp016976
456 Kanold PO, Manis PB (1999) Transient potassium currents regulate the discharge
457 patterns of dorsal cochlear nucleus pyramidal cells. J Neurosci 19:2195–2208. doi:
458 10.1523/JNEUROSCI.19-06-02195.1999
459 Kuo SP, Lu H-W, Trussell LO (2012) Intrinsic and synaptic properties of vertical cells of
460 the mouse dorsal cochlear nucleus. J Neurophysiol 108:1186–1198. doi:
461 10.1152/jn.00778.2011
462 Leao RM, Li S, Doiron B, Tzounopoulos T (2012) Diverse levels of an inwardly rectifying
463 potassium conductance generate heterogeneous neuronal behavior in a population
464 of dorsal cochlear nucleus pyramidal neurons. J Neurophysiol 107:3008–3019. doi:
465 10.1152/jn.00660.2011
466 Lorente de No R (1981) The Primary Acoustic Nuclei. Raven Press, NY
467 Madisen L, Mao T, Koch H, et al (2012) A toolbox of Cre-dependent optogenetic
468 transgenic mice for light-induced activation and silencing. Nat Neurosci 15:793–
469 802. doi: 10.1038/nn.3078
470 Manis PB (1990) Membrane properties and discharge characteristics of guinea pig
471 dorsal cochlear nucleus neurons studied in vitro. J Neurosci 10:2338–2351. doi:
472 10.1523/JNEUROSCI.10-07-02338.1990
473 Manis PB, Spirou GA, Wright DD, et al (1994) Physiology and morphology of complex

474 spiking neurons in the guinea pig dorsal cochlear nucleus. J Comp Neurol
475 348:261–276. doi: 10.1002/cne.903480208
476 Mugnaini E, Sekerková G, Martina M (2011) The unipolar brush cell: A remarkable
477 neuron finally receiving deserved attention. Brain Res Rev 66:220–245. doi:
478 10.1016/j.brainresrev.2010.10.001
479 Oertel D (1983) Synaptic responses and electrical properties of cells in brain slices of
480 the mouse anteroventral cochlear nucleus. J Neurosci 3:2043–2053. doi:
481 10.1523/JNEUROSCI.03-10-02043.1983
482 Oertel D, Wu SH, Garb MW, Dizack C (1990) Morphology and physiology of cells in
483 slice preparations of the posteroventral cochlear nucleus of mice. J Comp Neurol
484 295:136–154. doi: 10.1002/cne.902950112
485 Rao CR (1948) The Utilization of Multiple Measurements in Problems of Biological
486 Classification. J R Stat Soc Ser B 10:159–203. doi: 10.2307/2983775
487 Rothman JS, Manis PB (2003a) The roles potassium currents play in regulating the
488 electrical activity of ventral cochlear nucleus neurons. J Neurophysiol 89:3097–
489 3113. doi: 10.1152/jn.00127.2002
490 Rothman JS, Manis PB (2003b) Differential expression of three distinct potassium
491 currents in the ventral cochlear nucleus. J Neurophysiol 89:3070–3082. doi:
492 10.1152/jn.00125.2002
493 Street SE, Manis PB (2007) Action potential timing precision in dorsal cochlear nucleus
494 pyramidal cells. J Neurophysiol 97:4162–4172. doi: 10.1152/jn.00469.2006
495 Tavakoli A, Schmaltz A, Schwarz D, et al (2018) Quantitative Association of Anatomical
496 and Functional Classes of Olfactory Bulb Neurons. J Neurosci 38:7204–7220. doi:

497 10.1523/JNEUROSCI.0303-18.2018
498 Ting JT, Daigle TL, Chen Q, Feng G (2014) Acute brain slice methods for adult and
499 aging animals: Application of targeted patch clamp analysis and optogenetics.
500 Methods Mol Biol 1183:221–242. doi: 10.1007/978-1-4939-1096-0_14
501 Tripathy SJ, Burton SD, Geramita M, et al (2015) Brain-wide analysis of
502 electrophysiological diversity yields novel categorization of mammalian neuron
503 types. J Neurophysiol 113:3474–3489. doi: 10.1152/jn.00237.2015
504 Typlt M, Englitz B, Sonntag M, et al (2012) Multidimensional characterization and
505 differentiation of neurons in the anteroventral cochlear nucleus. PLoS One
506 7:e29965. doi: 10.1371/journal.pone.0029965
507 Weedman DL, Pongstaporn T, Ryugo DK (1996) Ultrastructural study of the granule cell
508 domain of the cochlear nucleus in rats: mossy fiber endings and their targets. J
509 Comp Neurol 369:345–360. doi: 10.1002/(SICI)1096-
510 9861(19960603)369:3<345::AID-CNE2>3.0.CO;2-5
511 Wu SH, Oertel D (1984) Intracellular injection with horseradish peroxidase of
512 physiologically characterized stellate and bushy cells in slices of mouse
513 anteroventral cochlear nucleus. J Neurosci 4:1577–1588. doi:
514 10.1523/JNEUROSCI.04-06-01577.1984
515 Xie R, Manis PB (2017) Radiate and Planar Multipolar Neurons of the Mouse
516 Anteroventral Cochlear Nucleus: Intrinsic Excitability and Characterization of their
517 Auditory Nerve Input. Front Neural Circuits 11:77. doi: 10.3389/fncir.2017.00077
518 Xie R, Manis PB (2013) Target-Specific IPSC Kinetics Promote Temporal Processing in
519 Auditory Parallel Pathways. J Neurosci 33:1598–1614. doi:

10.1523/JNEUROSCI.2541-12.2013

Zhang S, Oertel D (1993a) Cartwheel and superficial stellate cells of the dorsal cochlear nucleus of mice: intracellular recordings in slices. J Neurophysiol 69:1384–1397. doi: 10.1152/jn.1993.69.5.1384

Zhang S, Oertel D (1993b) Giant cells of the dorsal cochlear nucleus of mice: intracellular recordings in slices. J Neurophysiol 69:1384–1397. doi: 10.1152/jn.1993.69.5.1398

Zhang S, Oertel D (1994) Neuronal circuits associated with the output of the dorsal cochlear nucleus through fusiform cells. J Neurophysiol 71:914–930. doi: 10.1152/jn.1994.71.3.914

Zhang S, Oertel D (1993c) Tuberculoventral cells of the dorsal cochlear nucleus of mice: intracellular recordings in slices. J Neurophysiol 69:1409–1421. doi: 8389823

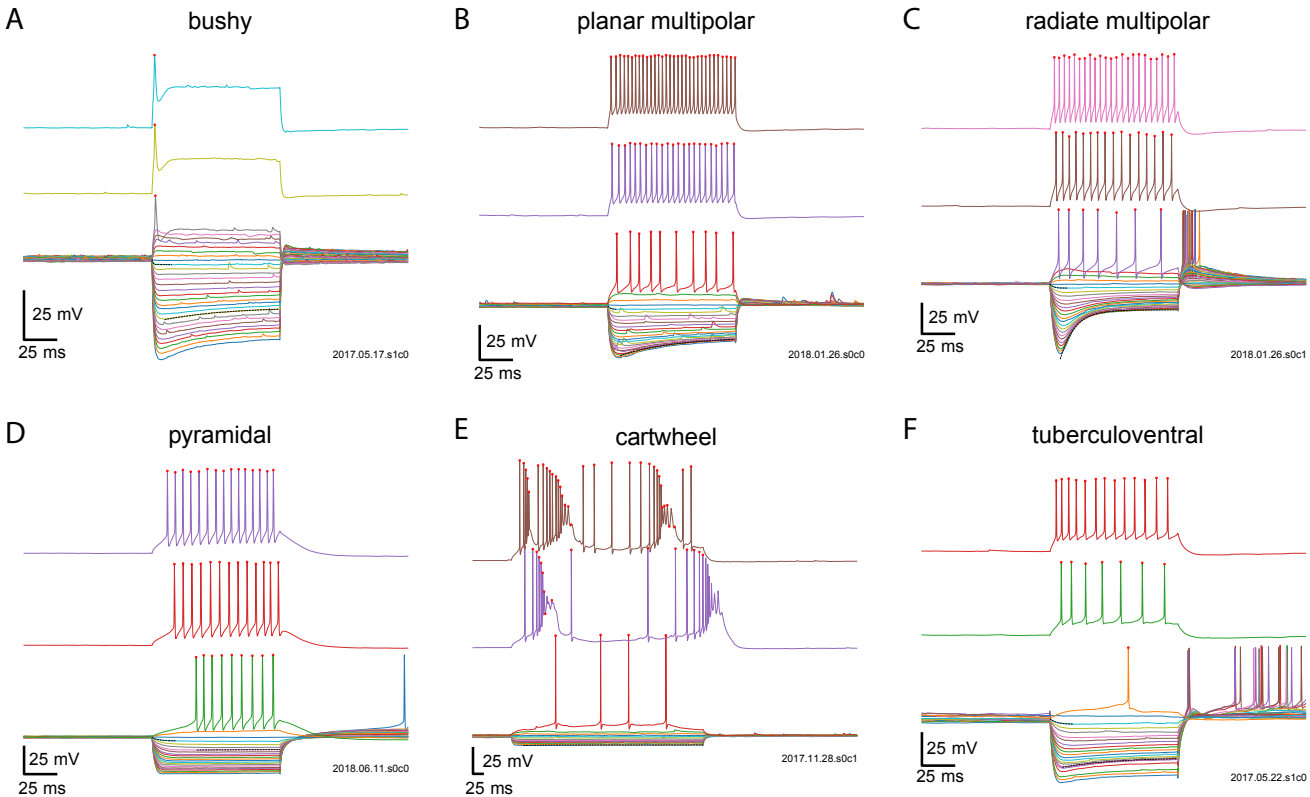
A
bushy
25 mV
25 ms
2017.05.17.s1c0
B
planar multipolar
25 mV
25 ms
2018.01.26.s0c0
C
radiate multipolar
25 mV
25 ms
2018.01.26.s0c1
D
pyramidal
25 mV
25 ms
2018.06.11.s0c0
E
cartwheel
25 mV
25 ms
2017.11.28.s0c1
F
tuberculoventral
25 mV
25 ms
2017.05.22.s1c0

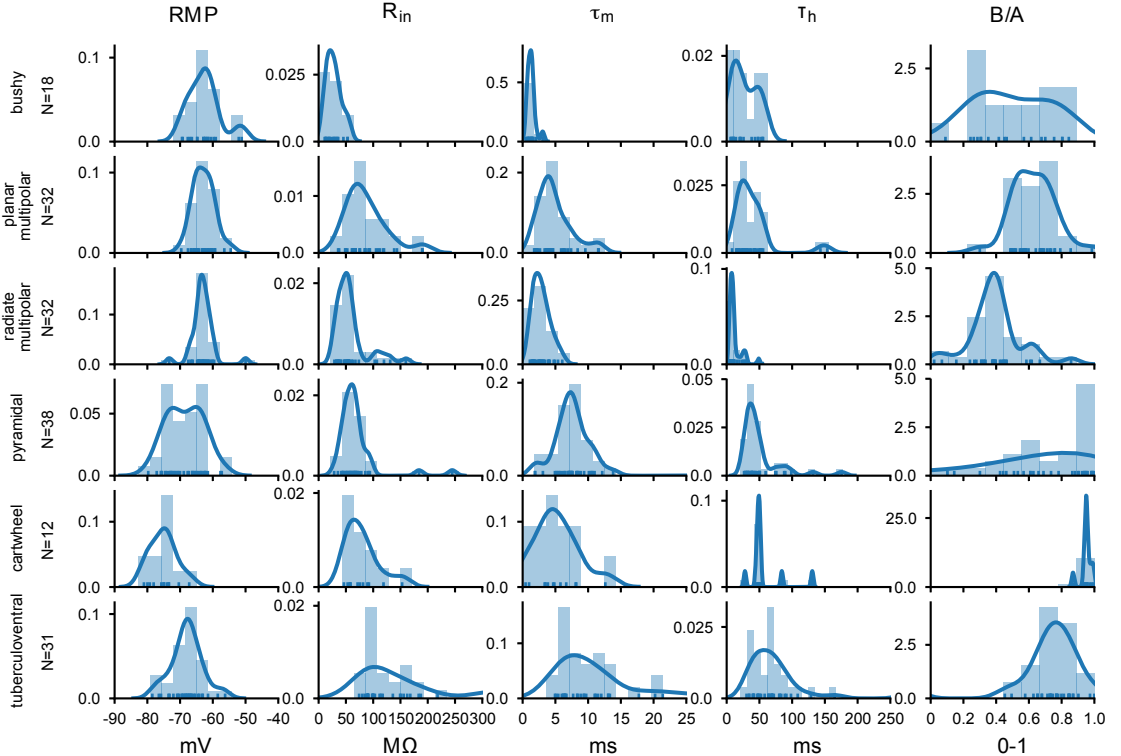
RMP
R_{in}
τ_m
τ_h
B/A
bushy N=18
planar multipolar N=32
radiate multipolar N=32
pyramidal N=38
cartwheel N=12
tuberculoventral N=31
mV
MΩ
ms
ms
0-1

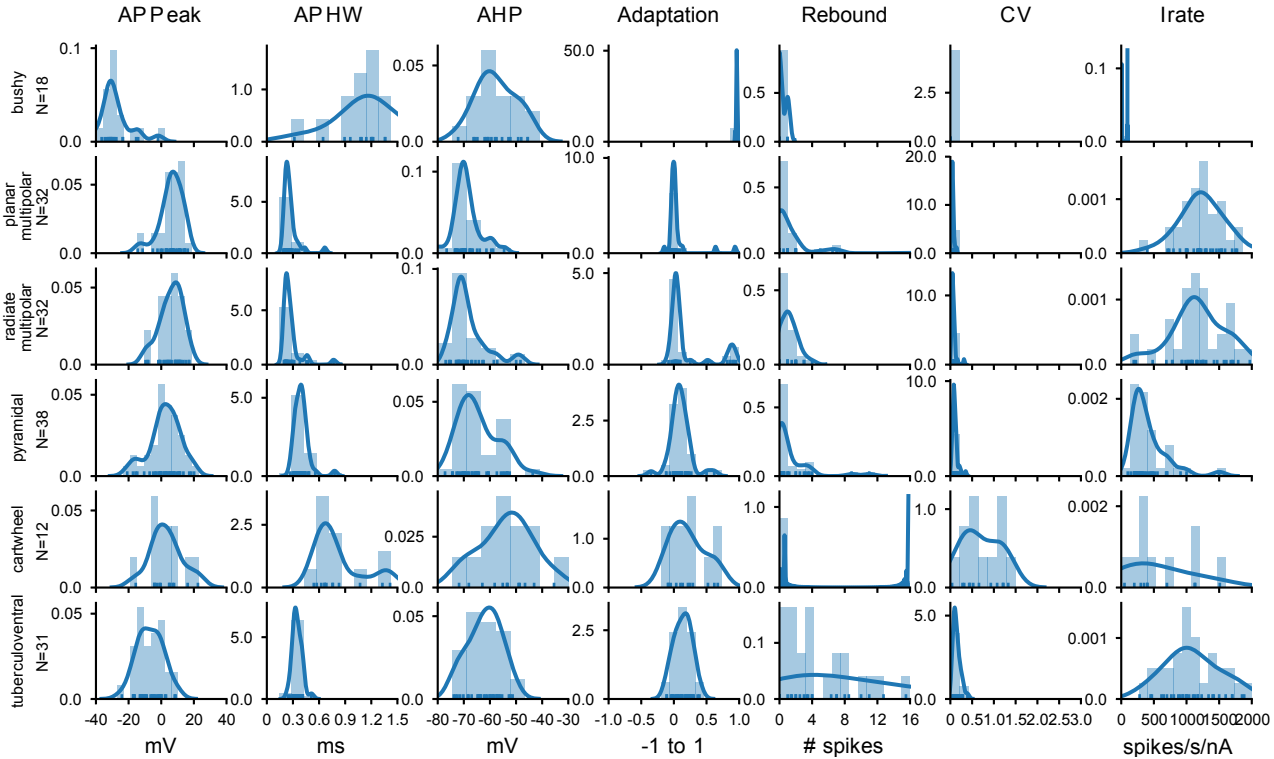
AP Peak
AP HW
AHP
Adaptation
Rebound
CV
Irate
bushy N=18
planar multipolar N=32
radiate multipolar N=32
pyramidal N=38
cartwheel N=12
tuberculoventral N=31
mV
ms
mV
-1 to 1
spikes
spikes/s/nA

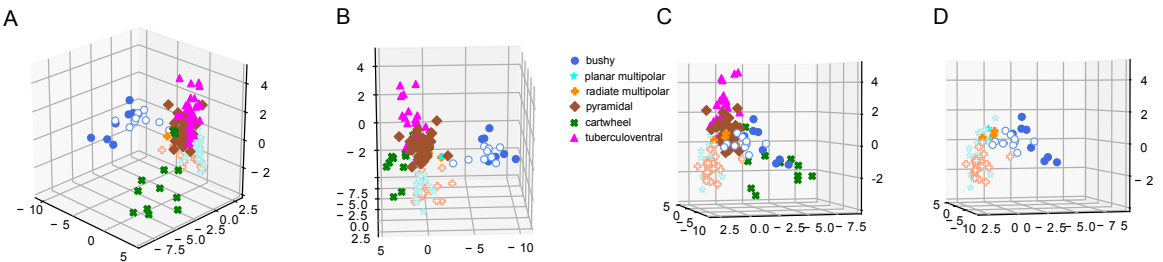
A
B
C
D
bushy
planar multipolar
radiate multipolar
pyramidal
cartwheel
tuberculoventral

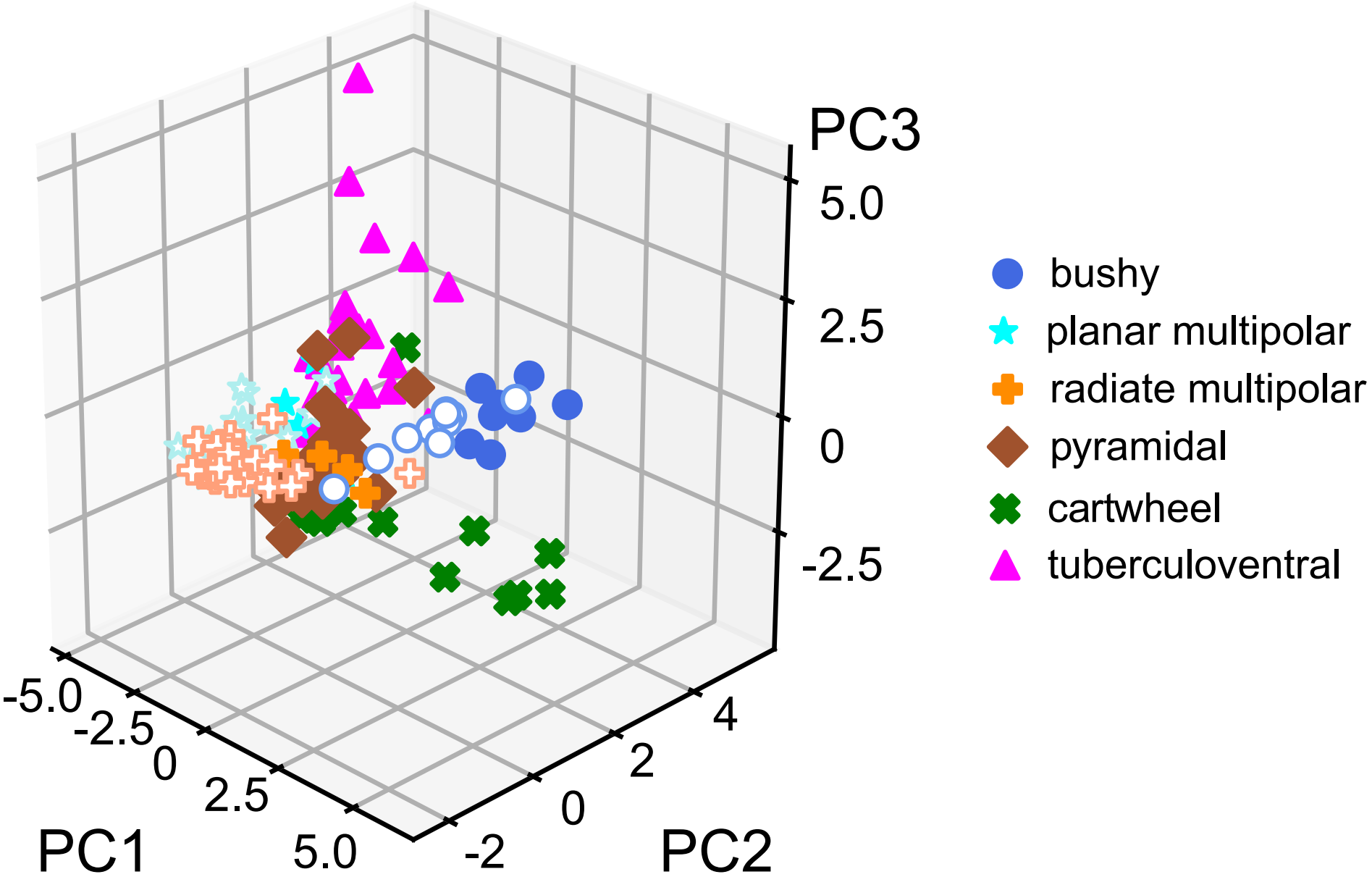
PC3
5.0
2.5
0
-2.5
-5.0
-2.5
0
2.5
5.0
PC1
-2
0
2
4
PC2
bushy
planar multipolar
radiate multipolar
pyramidal
cartwheel
tuberculoventral

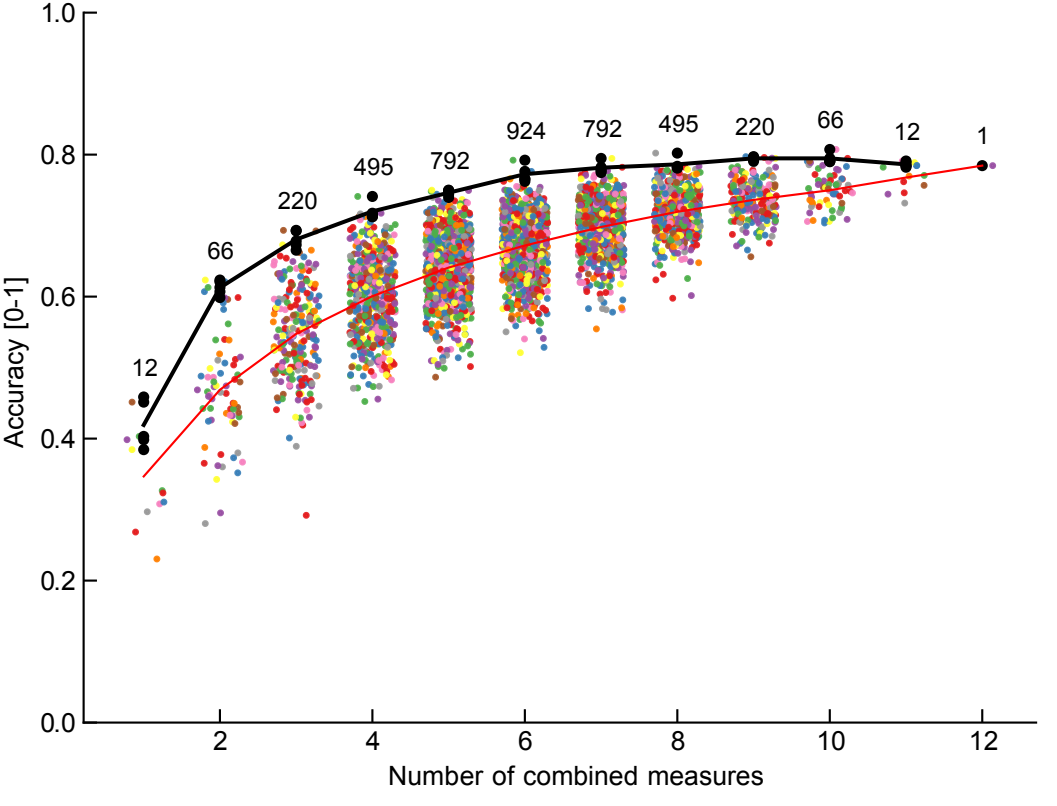
1.0
0.8
0.6
0.4
0.2
0.0
Accuracy [0-1]
2
4
6
8
10
12
Number of combined measures
12
66
220
495
792
924
792
495
220
66
12
1

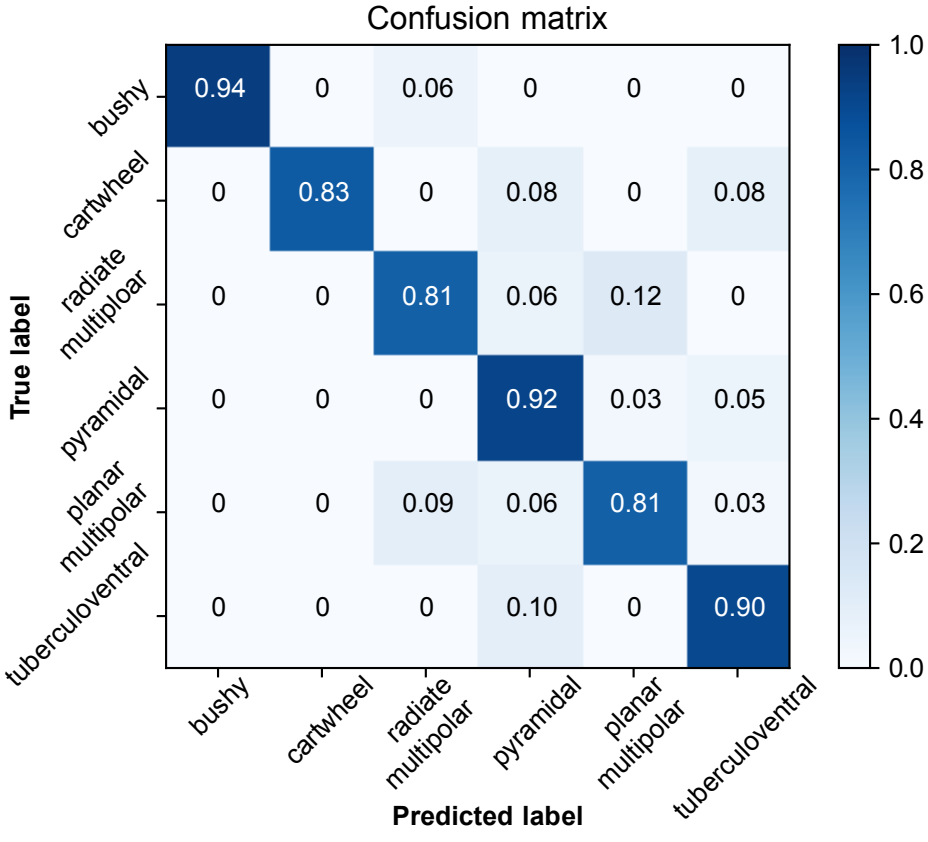
Confusion matrix
True label
Predicted label
bushy
cartwheel
radiate multiploar
pyramidal
planar multipolar
tuberculoventral
0.94 0 0.06 0 0 0
0 0.83 0 0.08 0 0.08
0 0 0.81 0.06 0.12 0
0 0 0 0.92 0.03 0.05
0 0 0.09 0.06 0.81 0.03
0 0 0 0.10 0 0.90
1.0
0.8
0.6
0.4
0.2
0.0